Supplement

S1 Data used for front line delineation

Table S1: Data used for mapping the front positions in Fig. 1, 2, 3 and 6.

Year	Platform	Reference	Date
1966	Aerial photography	Ferrigno, 2008	11/12 1966
1974	Landsat-1	Ferrigno, 2008	1974-01-06
1989	Landsat-3	Ferrigno, 2008	1989-02-20
1994	ERS-1/2		1994-02-01
1995	ERS-1/2		1995-10-27
1996	ERS-1/2		1996-02-10
1997	ERS-1/2		1997-01-29
1998	ERS-1/2		1998-01-30
1999	ERS-1/2		1999-11-10
2000	ERS-1/2		2000-02-20
2001	Landsat-7		2001-01-04
2002	ERS-1/2		2002-02-23
2003	ERS-1/2		2003-01-24
2004	ERS-1/2		2004-03-03
2005	ERS-1/2		2005-01-28
2007	ERS-1/2		2007-02-02
2008	Envisat	Wendt et al., 2010	2008-04-13
2009	ASTER	Wendt et al., 2010	2009-02-02
2010	ERS-1/2		2010-02-26
2011	TSX/TDX		2011-11-23
2012	TSX/TDX		2012-10-16
2013	TSX/TDX		2013-12-08
2014	TSX/TDX		2014-11-03
2015	Sentinel 1a		2015-09-09
2016	Sentinel 1a		2016-01-31

S2 Error estimation of surface velocity measurements

The corresponding errors of the velocity measurements were estimated as described in detail in Seehaus et al. (2015). It is assumed that the resulting uncertainties for each velocity field are induced by two major sources: the coregistration process and the tracking algorithm itself. The error caused by residual inaccuracies of the coregistration (σ_V^C) was determined by calculating the median velocity for 19 to 64 points on stable non-moving surfaces (e.g. rock outcrops) (Fig. S1). The error induced by the tracking algorithm (σ_V^T) was estimated according to the following formula, modified from McNabb et al. (2012):

$$\sigma_V^T = \frac{C\Delta x}{z\Delta t} \quad (1)$$

where C is the uncertainty of the tracking algorithm (assumed to be 0.4 pixels), Δx is the image resolution (mean values for each sensor are listed in Tab. S2), z is the oversampling factor (we applied a factor of two) and Δt is the temporal baseline between the SAR images. The total error (σ_V) of the velocity measurement is the sum of σ_V^C and σ_V^T. Table S3 lists the values Δt, σ_V^C, σ_V^T and σ_V for each velocity field. As in Seehaus et al. (2015) the quite large σ_V^T values for ERS-1/2 measurements during one of the sensor`s “Tandem” or “Ice Phases”, where the satellites orbited in 1- or 3-day repeat passes, were excluded from our estimation of σ_V.

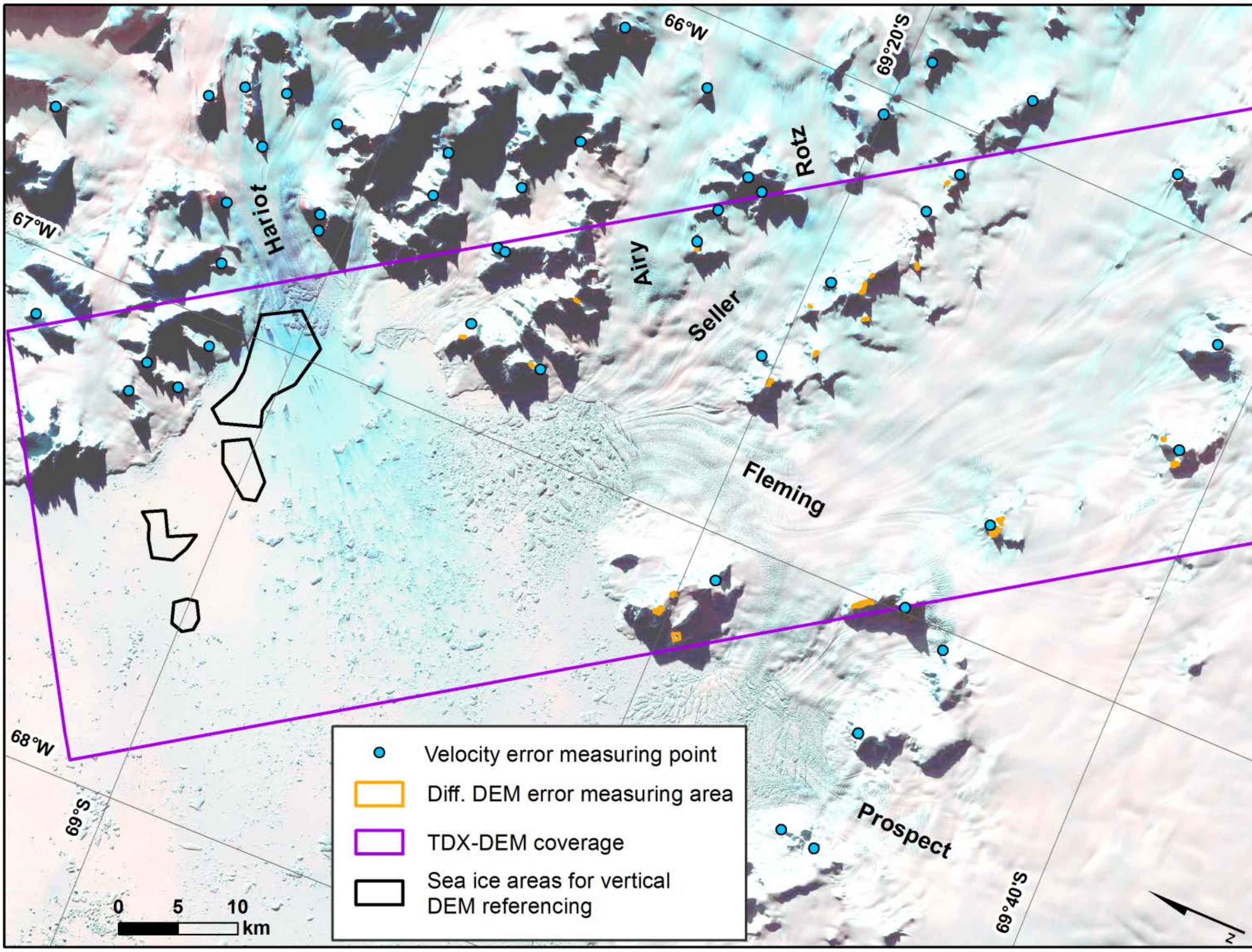

Figure S1: Stable points used for the coregistration error estimation of the intensity tracking results, stable areas on nunataks and hills for accuracy assessment of elevation change measurements and spatial coverage of the TanDEM-X DEMs. Background: Mosaic of two Landsat-8 „Natural Color“ images, acquired on September 16, 2015 ©USGS.

Table S2: Mean values of image resolution (Δx) at the study site used for the calculation of the velocity error induced by the tracking algorithm for each sensor. The tracking was done in slant range geometry without applying multilooking. For all sensors except for Sentinel-1a the ground resolution in range direction was coarser than in azimuth direction. Consequently a calculated mean value of the azimuth resolution was taken as upper bound approximation of Δx for Sentinel-1a tracking results and a mean value of the ground range resolution for the results obtained from data of the other sensors.

Sensor	Δx [m]
AMI SAR (ERS-1/2)	20
R1 (Radarsat 1)	20
ASAR (Envisat)	17
PALSAR (ALOS)	7
TSX/TDX(TerraSAR-X/TanDEM-X)	2
S1 (Sentinel-1a)	14

Table S3: Uncertainty σ_V of processed velocity fields. Date: Mean date of SAR acquisitions; Δt: Time interval in days between repeat SAR acquisitions; σ_V^C: Uncertainty of image coregistration; σ_V^T: Uncertainty of intensity tracking processing; ERS velocity fields with $\Delta t \leq$ 3d: σ_V = σ_V^C. The table is continued on the next pages.

Date [yyyy-mm-dd]	Sensor	Δt [d]	σ_V^C [m d^{-1}]	σ_V^T [m d^{-1}]	σ_V [m d^{-1}]
1994-01-27	AMI SAR	3	0.13	1.33	0.13
1994-02-05	AMI SAR	3	0.19	1.33	0.19
1994-02-23	AMI SAR	3	0.14	1.33	0.14
1994-02-26	AMI SAR	3	0.34	1.33	0.34
1994-03-07	AMI SAR	3	0.2	1.33	0.2
1995-10-27	AMI SAR	1	0.25	4	0.25
1996-02-09	AMI SAR	35	0.12	0.11	0.23
1997-02-27	AMI SAR	35	0.12	0.11	0.23
2000-09-19	R1	24	0.11	0.14	0.25
2000-10-13	R1	24	0.11	0.14	0.25
2002-12-02	AMI SAR	35	0.19	0.11	0.3
2003-01-06	AMI SAR	35	0.13	0.11	0.24
2003-10-22	R1	24	0.12	0.14	0.26
2003-11-15	R1	24	0.19	0.14	0.33
2003-12-09	R1	24	0.09	0.14	0.23
2004-02-19	R1	24	0.08	0.14	0.22
2004-03-14	R1	24	0.12	0.14	0.26
2004-04-07	R1	24	0.17	0.14	0.31
2004-09-22	R1	24	0.1	0.14	0.24
2004-10-16	R1	24	0.21	0.14	0.35
2004-11-09	R1	24	0.09	0.14	0.23
2004-12-03	R1	24	0.14	0.14	0.28
2004-12-27	R1	24	0.15	0.14	0.29
2005-01-20	R1	24	0.26	0.14	0.4
2005-02-13	R1	24	0.07	0.14	0.21
2005-04-26	R1	24	0.19	0.14	0.33
2005-10-11	R1	24	0.13	0.14	0.27
2005-11-04	R1	24	0.17	0.14	0.31
2006-01-15	R1	24	0.12	0.14	0.26
2006-02-08	R1	24	0.16	0.14	0.3
2006-02-15	ASAR	35	0.15	0.11	0.26
2006-03-04	R1	24	0.06	0.14	0.2

Date	Sensor	Δt	σ_V^C	σ_V^T	σ_V
[yyyy-mm-dd]		[d]	[m d^{-1}]	[m d^{-1}]	[m d^{-1}]
2006-03-28	R1	24	0.23	0.14	0.37
2006-04-21	R1	24	0.17	0.14	0.31
2006-05-31	ASAR	35	0.09	0.11	0.2
2006-07-05	ASAR	35	0.11	0.11	0.22
2006-07-18	PALSAR	46	0.06	0.03	0.09
2006-08-09	ASAR	35	0.14	0.11	0.25
2006-11-03	AMI SAR	35	0.18	0.11	0.29
2007-04-10	ASAR	35	0.17	0.11	0.28
2007-05-15	ASAR	35	0.06	0.11	0.17
2007-05-16	ASAR	35	0.09	0.11	0.2
2007-06-19	ASAR	35	0.05	0.11	0.16
2007-06-20	ASAR	35	0.08	0.11	0.19
2007-07-25	ASAR	35	0.05	0.11	0.16
2007-08-28	ASAR	35	0.1	0.11	0.21
2007-08-29	ASAR	35	0.13	0.11	0.24
2007-10-02	ASAR	35	0.08	0.11	0.19
2007-10-03	ASAR	35	0.11	0.11	0.22
2007-10-23	PALSAR	46	0.05	0.03	0.08
2007-11-06	ASAR	35	0.06	0.11	0.17
2008-01-05	R1	24	0.2	0.14	0.34
2008-04-30	ASAR	35	0.11	0.11	0.22
2008-06-03	ASAR	35	0.08	0.11	0.19
2008-07-08	ASAR	35	0.06	0.11	0.17
2008-08-12	ASAR	35	0.08	0.11	0.19
2008-09-16	ASAR	35	0.08	0.11	0.19
2008-10-21	ASAR	35	0.07	0.11	0.18
2009-02-06	PALSAR	46	0.15	0.03	0.18
2009-04-14	ASAR	35	0.22	0.11	0.33
2009-07-29	ASAR	35	0.09	0.11	0.2
2009-09-02	ASAR	35	0.09	0.11	0.2
2009-10-07	ASAR	35	0.09	0.11	0.2
2010-02-08	ASAR	35	0.08	0.11	0.19
2010-02-11	ASAR	35	0.19	0.11	0.3
2010-03-31	ASAR	35	0.09	0.11	0.2
2010-05-05	ASAR	35	0.1	0.11	0.21

Date [yyyy-mm-dd]	Sensor	Δt [d]	σ_V^C [m d^{-1}]	σ_V^T [m d^{-1}]	σ_V [m d^{-1}]
2010-06-09	ASAR	35	0.08	0.11	0.19
2010-07-14	ASAR	35	0.09	0.11	0.2
2010-08-18	ASAR	35	0.1	0.11	0.21
2010-09-22	ASAR	35	0.09	0.11	0.2
2010-10-27	TSX/TDX	33	0.01	0.01	0.02
2010-10-31	PALSAR	46	0.33	0.03	0.36
2010-11-18	TSX/TDX	11	0.02	0.04	0.06
2011-05-10	AMI SAR	3	0.25	1.33	0.25
2011-06-27	AMI SAR	3	0.36	1.33	0.36
2011-10-02	TSX/TDX	11	0.02	0.04	0.06
2011-11-15	TSX/TDX	11	0.03	0.04	0.07
2011-12-29	TSX/TDX	11	0.01	0.04	0.05
2012-03-15	TSX/TDX	11	0.02	0.04	0.06
2012-04-06	TSX/TDX	11	0.02	0.04	0.06
2012-04-17	TSX/TDX	11	0.02	0.04	0.06
2012-05-31	TSX/TDX	11	0.03	0.04	0.07
2012-06-11	TSX/TDX	11	0.01	0.04	0.05
2012-07-25	TSX/TDX	11	0.02	0.04	0.06
2012-09-07	TSX/TDX	11	0.02	0.04	0.06
2012-10-21	TSX/TDX	11	0.02	0.04	0.06
2012-12-04	TSX/TDX	11	0.02	0.04	0.06
2013-01-17	TSX/TDX	11	0.01	0.04	0.05
2013-03-13	TSX/TDX	11	0.03	0.04	0.07
2013-03-23	TSX/TDX	11	0.08	0.04	0.12
2013-04-15	TSX/TDX	11	0.03	0.04	0.07
2013-06-09	TSX/TDX	11	0.02	0.04	0.06
2013-06-20	TSX/TDX	11	0.02	0.04	0.06
2013-07-01	TSX/TDX	11	0.02	0.04	0.06
2013-07-12	TSX/TDX	11	0.02	0.04	0.06
2013-11-20	TSX/TDX	11	0.04	0.04	0.08
2013-12-13	TSX/TDX	11	0.03	0.04	0.07
2013-12-24	TSX/TDX	11	0.02	0.04	0.06
2014-01-26	TSX/TDX	11	0.01	0.04	0.05
2014-08-23	TSX/TDX	11	0.02	0.04	0.06
2014-09-03	TSX/TDX	11	0.03	0.04	0.07

Date [yyyy-mm-dd]	Sensor	Δt [d]	σ_V^C [m d^{-1}]	σ_V^T [m d^{-1}]	σ_V [m d^{-1}]
2014-12-11	TSX/TDX	11	0.01	0.04	0.05
2015-01-24	TSX/TDX	11	0.03	0.04	0.07
2015-09-03	S1	12	0.06	0.23	0.29
2015-09-15	S1	12	0.05	0.23	0.28
2015-10-21	S1	12	0.15	0.23	0.38
2015-12-08	S1	12	0.11	0.23	0.34
2015-12-20	S1	12	0.07	0.23	0.3
2016-01-01	S1	12	0.09	0.23	0.32
2016-01-13	S1	12	0.05	0.23	0.28
2016-01-25	S1	12	0.08	0.23	0.31
2016-02-06	S1	12	0.08	0.23	0.31
2016-02-18	S1	12	0.08	0.23	0.31
2016-03-01	S1	12	0.09	0.23	0.32
2016-03-13	S1	12	0.08	0.23	0.31
2016-04-06	S1	12	0.09	0.23	0.32
2016-04-18	S1	12	0.07	0.23	0.3
2016-06-05	S1	12	0.12	0.23	0.35
2016-07-23	S1	12	0.1	0.23	0.33
2016-08-04	S1	12	0.08	0.23	0.31
2016-08-16	S1	12	0.06	0.23	0.29

S3 Uncertainty estimation of variables for the hydrostatic height anomaly calculations and assessment of error propagation

In order to assess the propagation of uncertainties for the calculation of hydrostatic height anomalies we estimated the error of each variable of Formula 2. The accuracy of the ATM elevations was estimated to be ± 0.2 m. The overall uncertainty of the EIGEN-6C4 geoid is 0.24 m (http://icgem.gfz-potsdam.de/ICGEM/). Accounting for an unknown additional error induced by kriging of the geoid values, we assumed a total accuracy of ± 0.5 m for e. Following the recommendation of the CReSIS Radar Depth Sounders (RDS) user guide (ftp://data.cresis.ku.edu/data/rds/rds_readme.pdf) we defined the error of H_i as the sum of the RMS error of the sensor`s range resolution and the RMS error of the dielectric. Depending on the sensor, the uncertainty of H_i varies between ~6 and ~14 m for an ice thickness of 750 m, which is the approx. mean ice thickness in the vicinity of the current grounding line measured on our OIB profiles. For ρ_i we used a value of 917 kg m^{-3}, which is the standard density of pure ice (Benn and Evans, 2013). However, since impurities in the ice can cause this value to vary by around ± 5 kg m^{-3} (Griggs and Bamber, 2011), we chose this rate to be the uncertainty of ρ_i. The global mean density of sea water is 1027 kg m^{-3}, but this value can vary locally. According to Griggs and Bamber (2011) we therefore assumed an error of ± 5 kg m^{-3} for ρ_w. The firn density correction factor for pure glacier ice is 0. In situ values of about 10 m have been measured for δ on Larsen C Ice Shelf (Griggs and Bamber, 2009) and firn density correction factors > 20 m have been reported for areas of convergent flow on the Ross Ice Shelf (Bamber and Bentley, 1994). Since δ can vary spatially and we had no information on firn densities on the Airy-Rotz-Seller-Fleming glacier system, we used a mean firn density correction factor of 10 m throughout our calculations and noted an uncertainty of ± 10 m. In order to quantify the total error of Δe and to consider the propagation of uncertainties, we run a Monte Carlo simulation based on Formula 1 and 2 with 100.000 runs. For all possible sensor-depending errors of H_i=750 m the Monte Carlo simulation yielded a standard deviation of < 12 m for Δe. Thus we assumed the total error of Δe to be ± 12 m. Consequently, we assigned locations on our OIB and PIB profiles to be freely floating ice, if the calculated values of Δe lay within this range.

S4 Penetration bias correction of TSX/TDX 2011 – 2014 elevation change rates

Figure S4 a-c: Penetration bias correction of TSX/TDX 2011 – 2014 elevation change rates

(a) Comparison of yearly elevation change rates obtained from OIB ATM LiDAR measurements (2011-11-17/2014-11-10) and TSX/TDX DEMs (2011-11-21/2014-11-03) after vertical registration of the TSX/TDX DEMs. Data is plotted against absolute ellipsoidal elevations from the resampled Bedmap 2 DEM (Fretwell et al., 2013). Grey dots: elevation change rates between 2011 and 2014 from OIB ATM. Black line: cubic function fitted to the OIB ATM measurements. Light blue dots: elevation change rates between 2011 and 2014 from TSX/TDX. Blue line: cubic function fitted to the TSX/TDX measurements

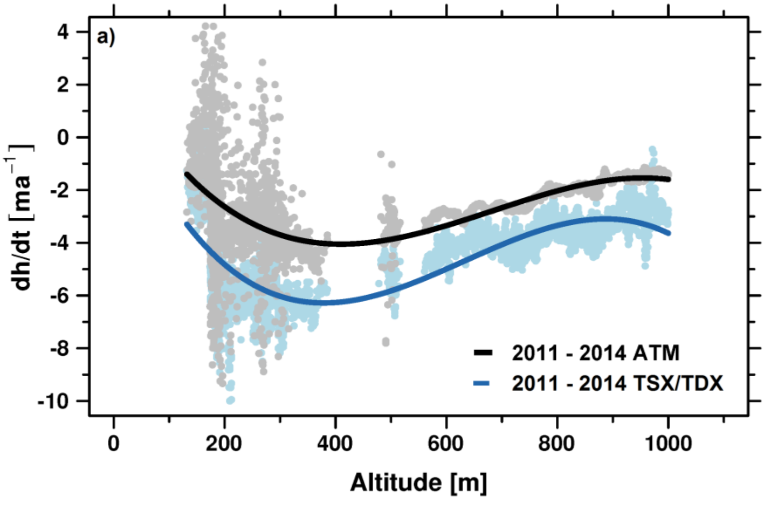

(b) Penetration bias correction model for TSX/TDX change rates. Data is plotted against absolute ellipsoidal elevations from the resampled Bedmap 2 DEM (Fretwell et al., 2013). Black dots: differences between TSX/TDX elevation change rates (r_{DEM}) and OIB ATM rates (r_{ATM}). Green line local polynomial model fitted to the measurements.

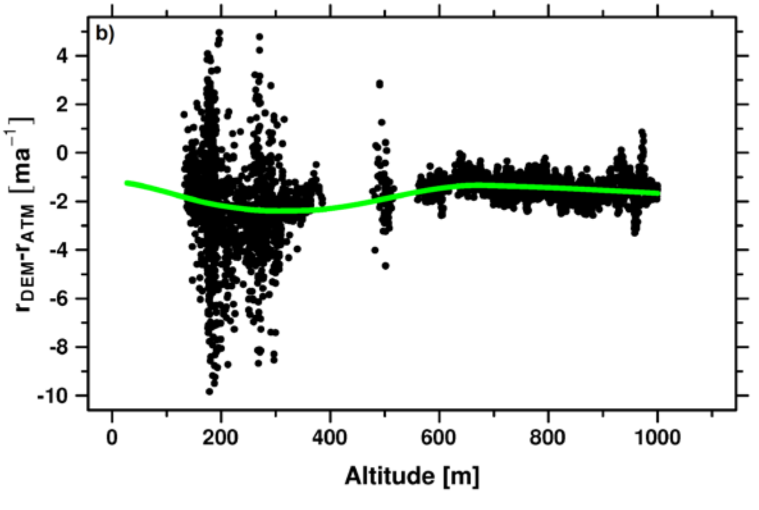

(c) Comparison of yearly elevation change rates obtained from OIB ATM LiDAR measurements (2011-11-17/2014-11-10) and TSX/TDX DEMs (2011-11-21/2014-11-03) after vertical registration and penetration depth bias correction of the TSX/TDX elevation change map. Data is plotted against absolute ellipsoidal elevations from the resampled Bedmap 2 DEM (Fretwell et al., 2013). Grey dots: elevation change rates between 2011 and 2014 from OIB ATM. Black line: cubic function fitted to the OIB ATM measurements. Light blue dots: elevation change rates between 2011 and 2014 from TSX/TDX. Blue line: cubic function fitted to the TSX/TDX measurements

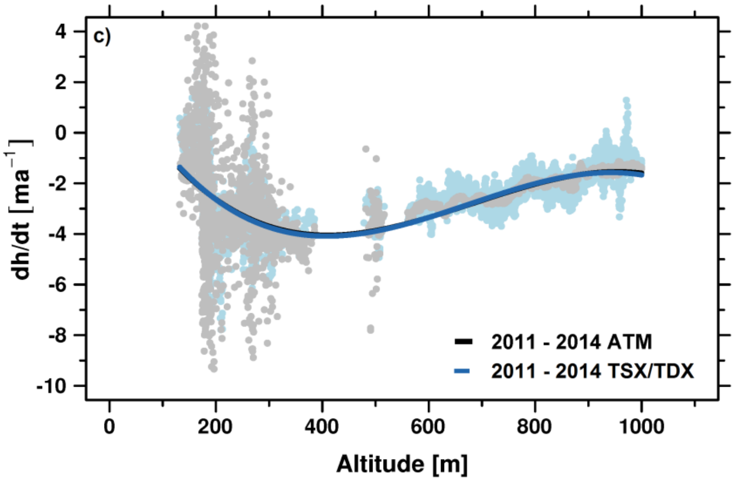

S5 Results of the hydrostatic height anomaly calculations

Figure S5 a-e: Fulfillment of the hydrostatic equilibrium assumption from hydrostatic height anomaly calculations along PIB and OIB profiles. Profiles are to read from left to right (in upstream direction). Dates of PIB and OIB flights: a) 2002-11-26, b) 2004-11-18, c) 2011-11-17, d) 2014-11-16, e) 2014-11-10. Purple dots: PIB/OIB ice surface/bottom elevations. Brown line: Bedrock elevation from Huss and Farinotti, 2014. Yellow line: Bedrock elevation from Bedmap 2 (Fretwell et al., 2013). Red and blue dots: calculated ice surface elevation in hydrostatic equilibrium e_{he} and information on hydrostatic equilibrium (blue: freely floating ice, red: grounded ice)

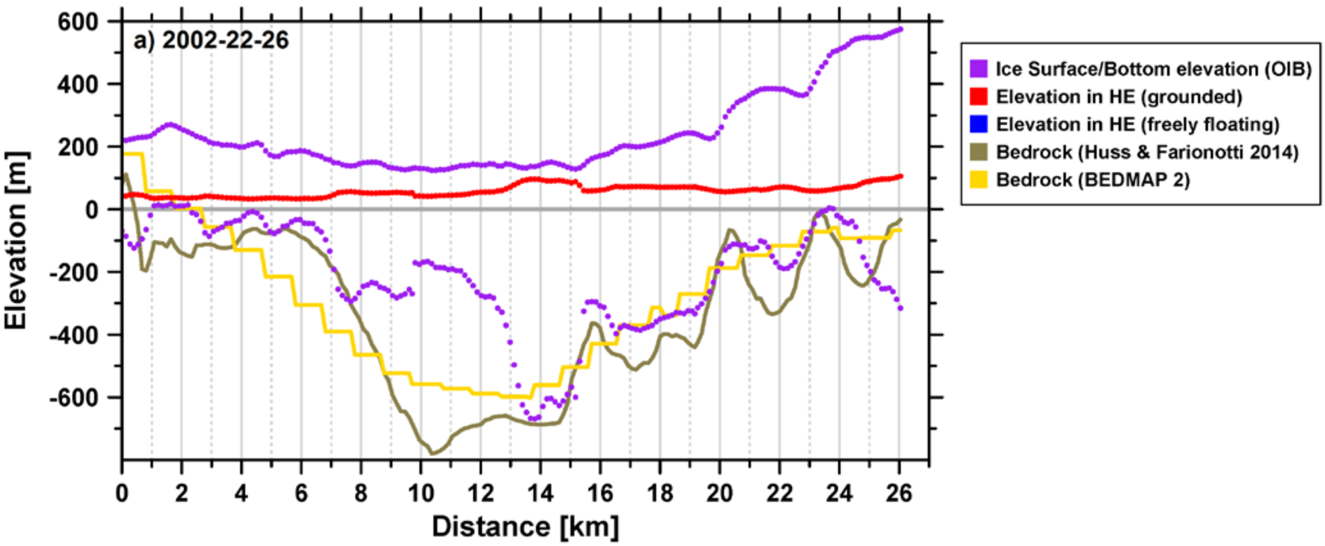

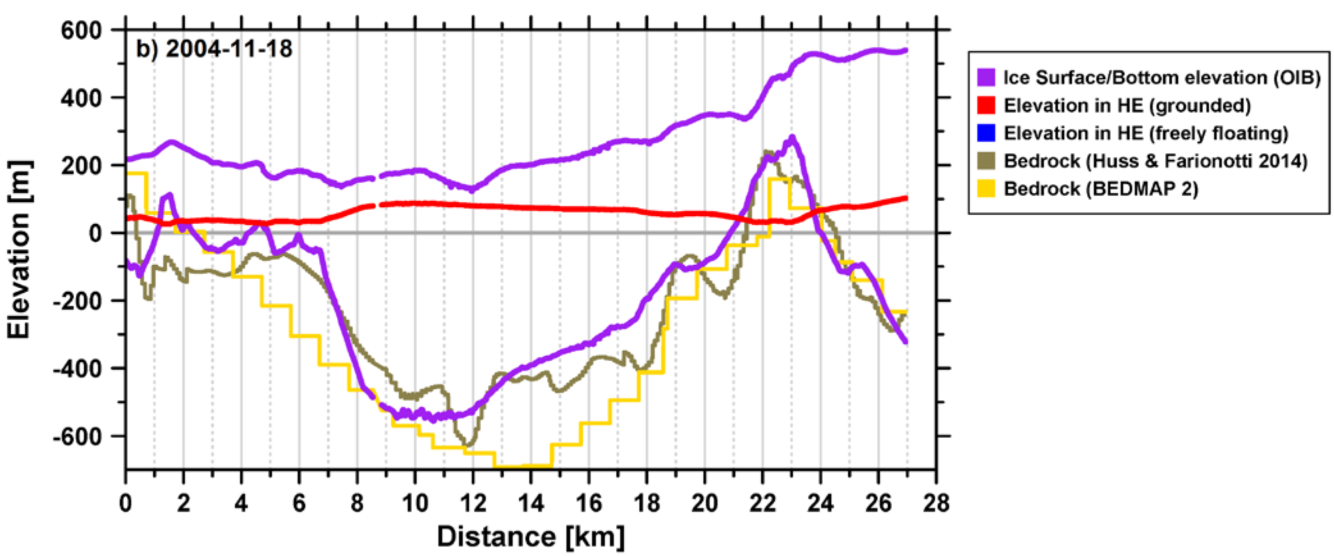

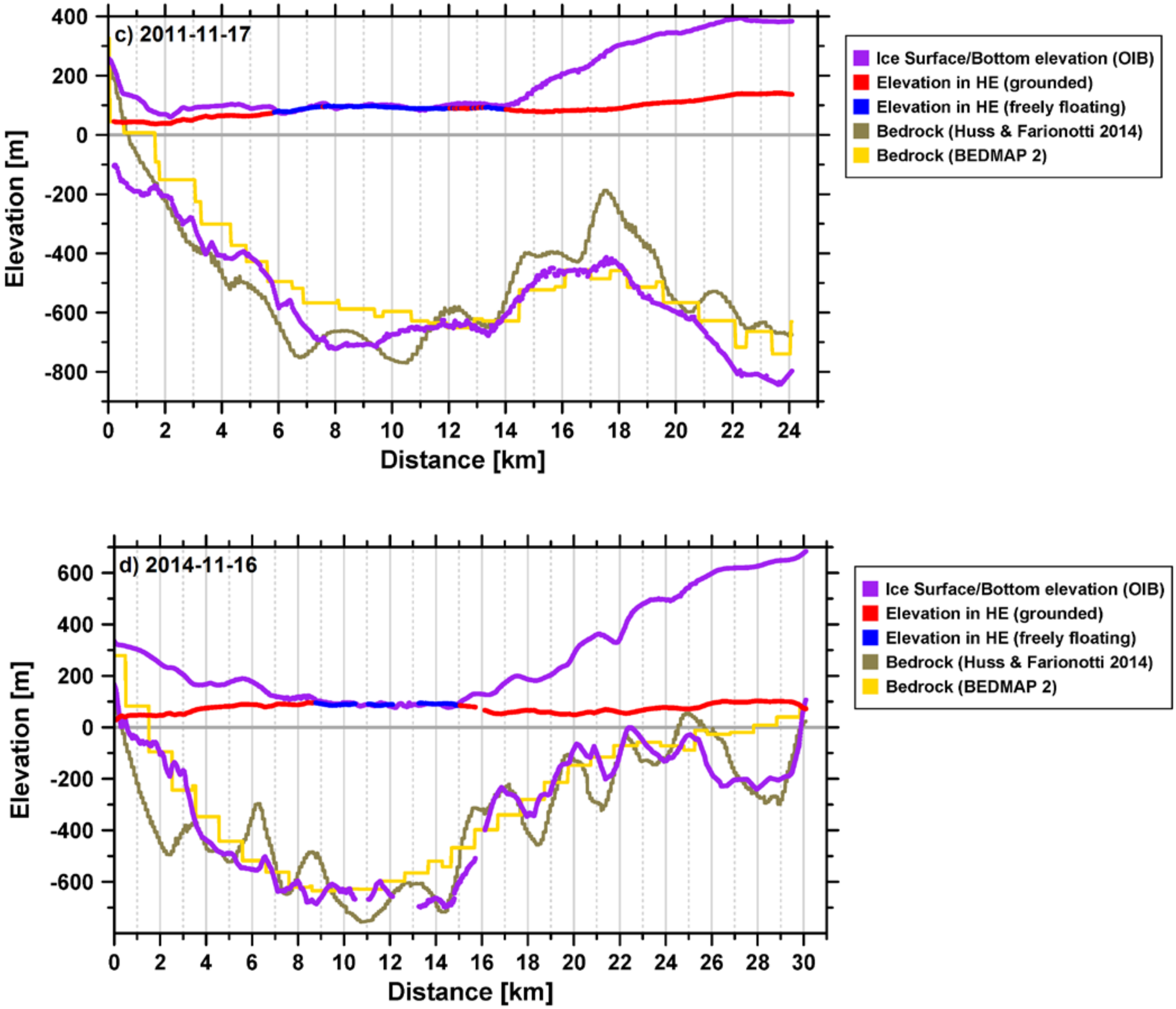
c) 2011-11-17
Elevation [m]
Distance [km]
Ice Surface/Bottom elevation (OIB)
Elevation in HE (grounded)
Elevation in HE (freely floating)
Bedrock (Huss & Farionotti 2014)
Bedrock (BEDMAP 2)
d) 2014-11-16
Elevation [m]
Distance [km]
Ice Surface/Bottom elevation (OIB)
Elevation in HE (grounded)
Elevation in HE (freely floating)
Bedrock (Huss & Farionotti 2014)
Bedrock (BEDMAP 2)

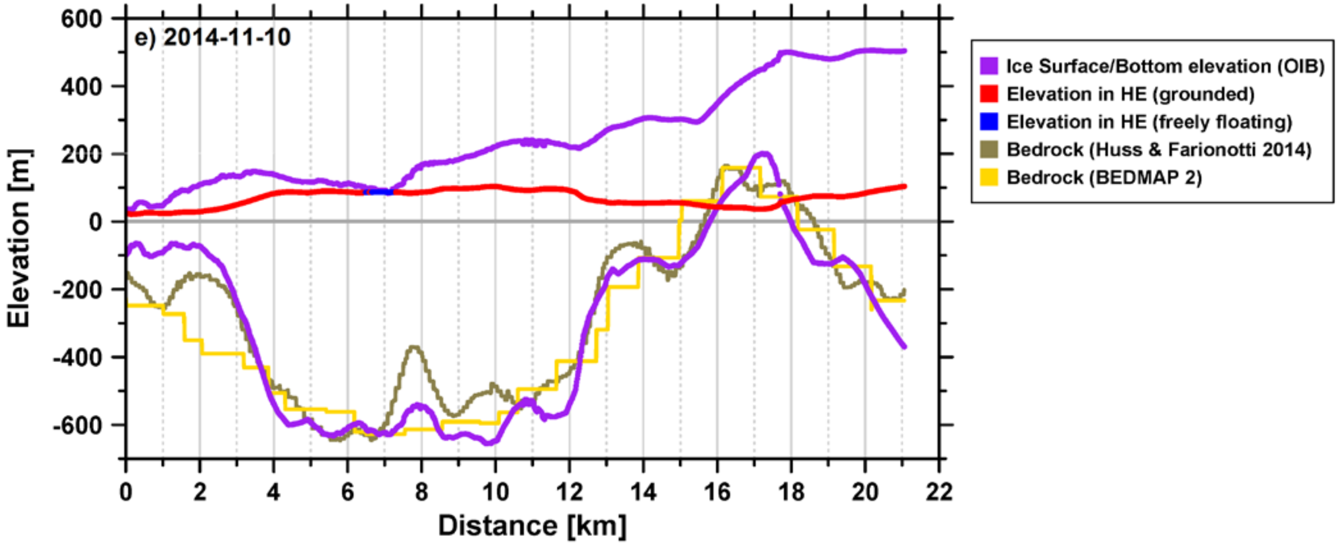
e) 2014-11-10
Ice Surface/Bottom elevation (OIB)
Elevation in HE (grounded)
Elevation in HE (freely floating)
Bedrock (Huss & Farionotti 2014)
Bedrock (BEDMAP 2)
Elevation [m]
Distance [km]
600
400
200
0
-200
-400
-600
0
2
4
6
8
10
12
14
16
18
20
22

S6 Estimation of grounding line positions along profiles of surface velocity, bedrock topography, ice elevations and hydrostatic height anomalies

Figure S6.1-4: Estimated grounding line positions on profiles 1-5 (for location see Fig. 6) based on surface velocities, elevation change rates, hydrostatic height anomalies, Distances for Fig. S6.1-4 are relative to the glacier front in 2007 (Fig. 6), OIB ice surface/bottom elevations and modeled bedrock topography (Fretwell et al., 2013; Huss and Farinotti, 2014). F: Front, grounding line: Grounding Line. Brown line: Bedrock elevation from Huss, Farinotti (2014). Yellow line: Bedrock elevation from Bedmap 2 (Fretwell et al. 2013). Green: freely floating ice, Red: partially floating/grounded ice, Blue lines: OIB/PIB ice surface/bottom elevations.

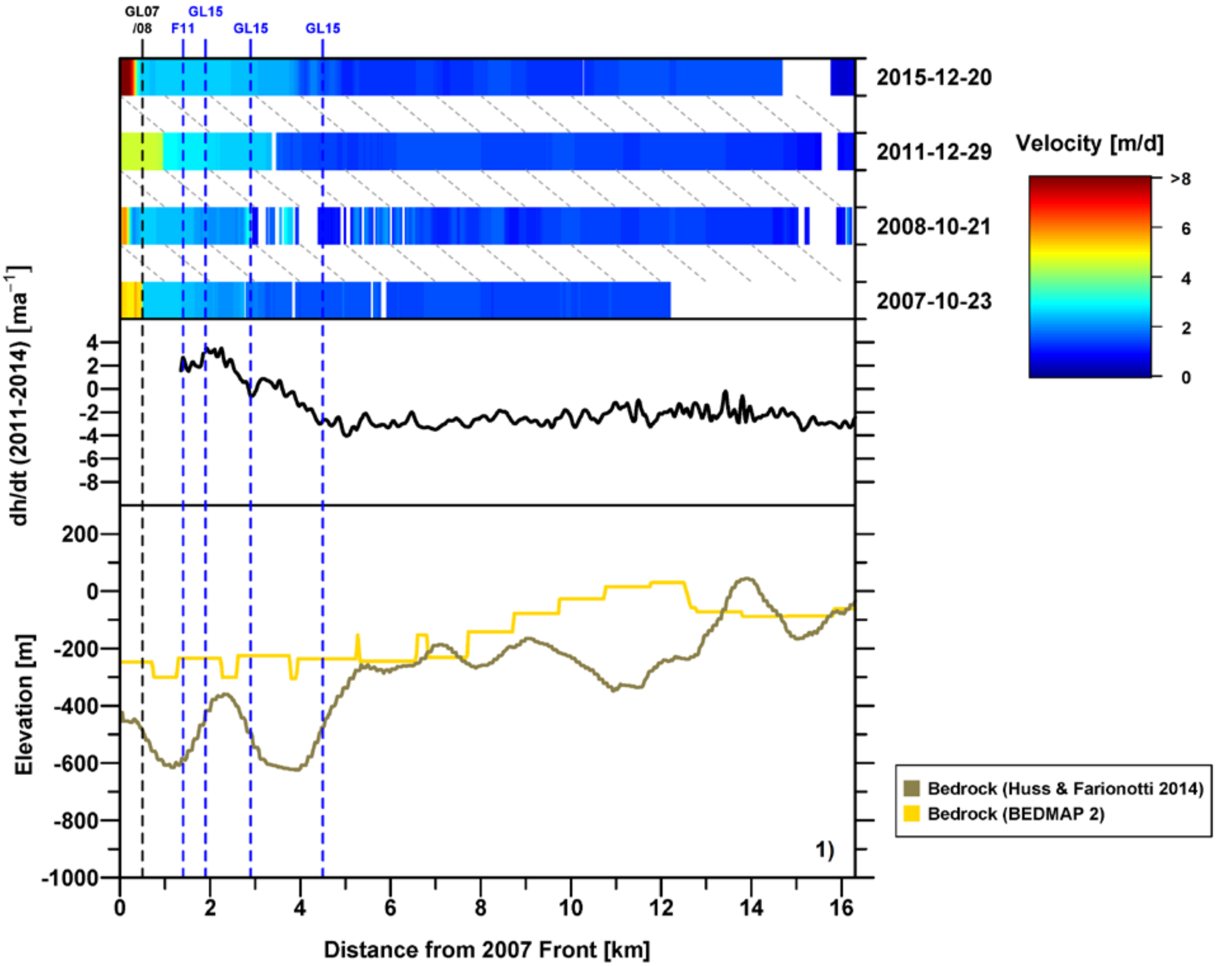

On Airy Glacier, velocity data extracted along the center line Profile 1 (Fig. 6) does not show signs of acceleration between 2007 and 2008. Furthermore the front in 2008 was directly located at the 1996/2007 grounding line. It is likely that at this time Airy Glacier was still grounded at the 1996/2007 grounding line position. However, in 2011 the front had retreated behind the 1996/2007 grounding line. Hydrostatic height anomalies in 2011 (Fig. 6,Track c) indicate that the ice is recently grounded on a hill, located ~2 km upstream, which reaches to the subglacial trough. However, 2011–2014 TSX/TDX elevation change rates as well as recent surface velocities point to a maximum upstream location of the current grounding line on Airy Glacier at the limit of the subglacial trough ~4-5 km upstream.

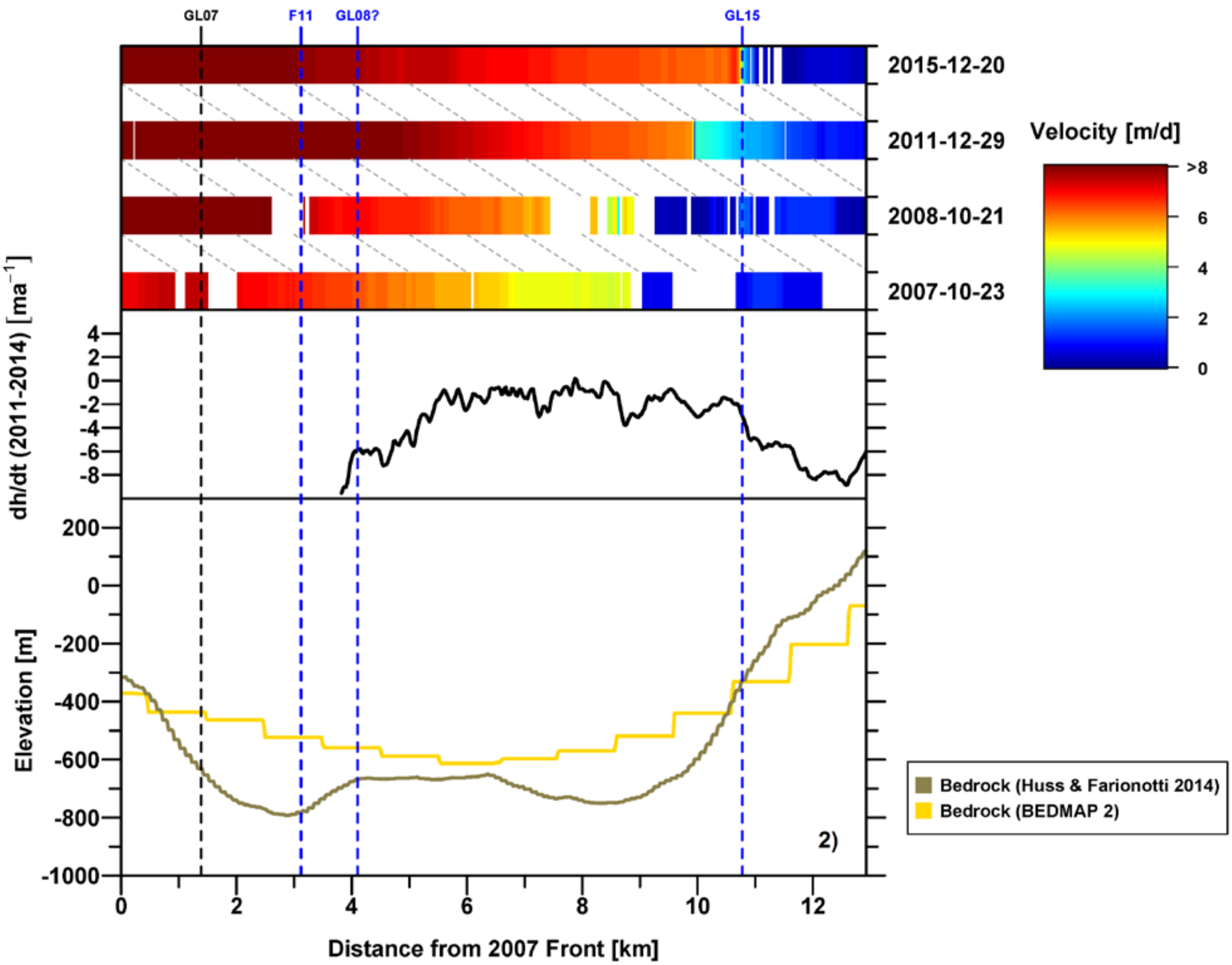

Close to the confluence of Fleming and Seller Glacier velocity data extracted along Profile 2 (Fig. 6) shows only slight acceleration between 2007 and 2008. Although it is difficult to tell where the grounding line exactly was in 2008 in this region, the data suggest that in 2008 the grounding line had not retreated until to the edge of the trough ~10-11 km upstream, yet. A conservative estimate would be that the grounding line in 2008 was located on a gentle hill close to the 2011 front, ~4 km upstream. In 2011 however, the glacier had substantially accelerated and in 2015 high velocities had further propagated inland along the profile. Taking into account elevation change rates and information from hydrostatic height anomaly calculations (Fig. 6, Track d), the grounding line position in 2011 was likely already located at the edge of the subglacial trough and had further retreated by ~1 km in 2015.

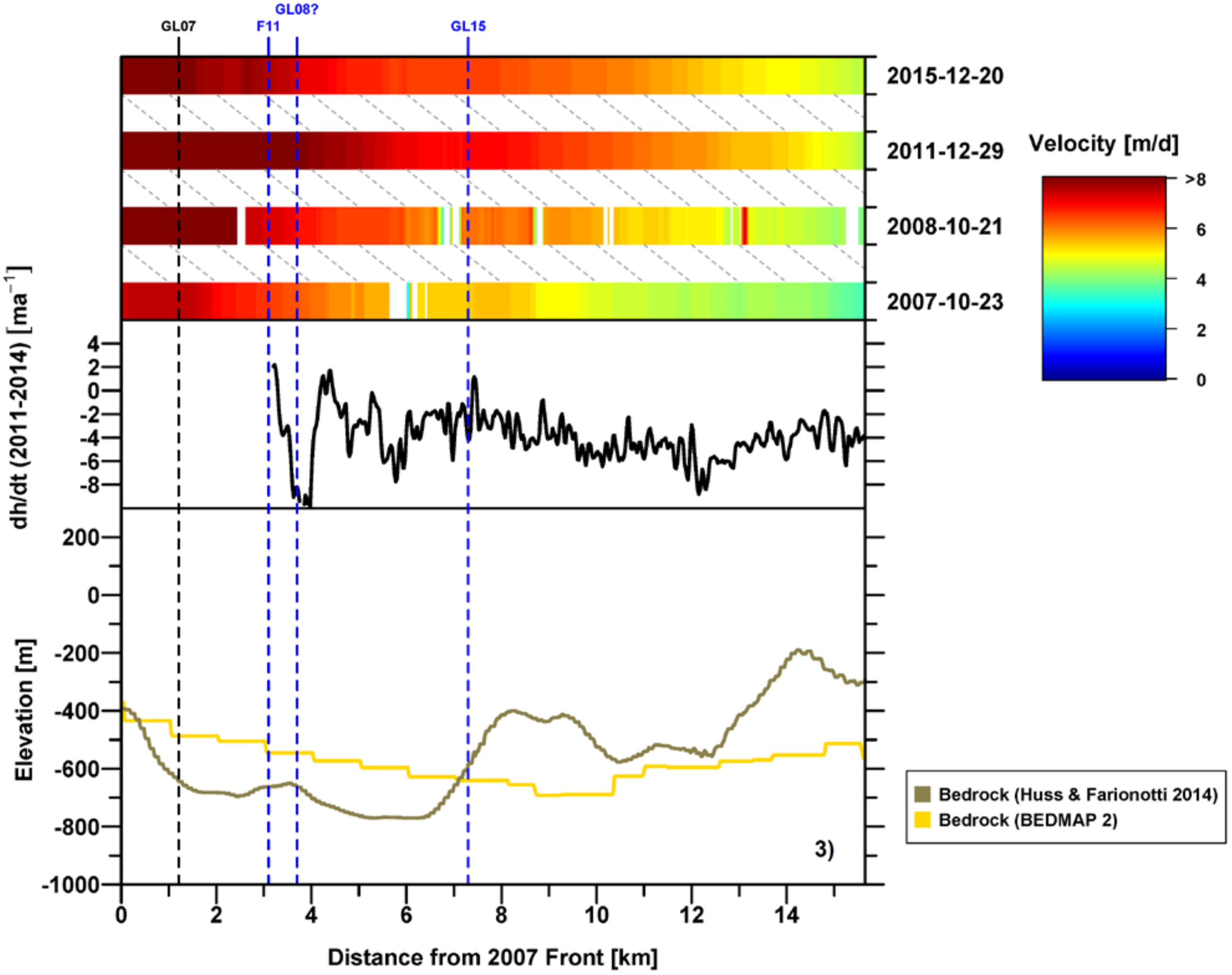

Velocities extracted along Profile 3 (Fig. 6) show an upstream propagation of high velocities between 2007 and 2008 of up to 12 km. This indicates that the grounding line had already migrated upstream from its 1996/2007 position in 2008. However, due to the limitations of estimating the grounding line based on velocity information only, the extent of the retreat in 2008 remains unclear. A possible grounding line position in 2008 is a smaller hill close to the front in 2011, ~4 km upstream of the front in 2007. In 2011 the glacier front had retreated behind the 1996/2007 grounding line. Although no clear pattern of lower ice elevation change rates is visible on the extracted 2011–2014 dh/dt data, hydrostatic height anomalies calculated for an OIB flight path in 2014 (Fig. 6, Track d) show that the glacier tongue downstream of the hill chain ~8 km upstream was freely floating in 2014. Although in 2011 high velocities had gradually propagated up to 14 km upstream of the front in 2007, OIB data acquired in 2014 (Fig. 6, Track e) reveal that the ice upstream of the hill chain at ~ 8 km is not freely floating.

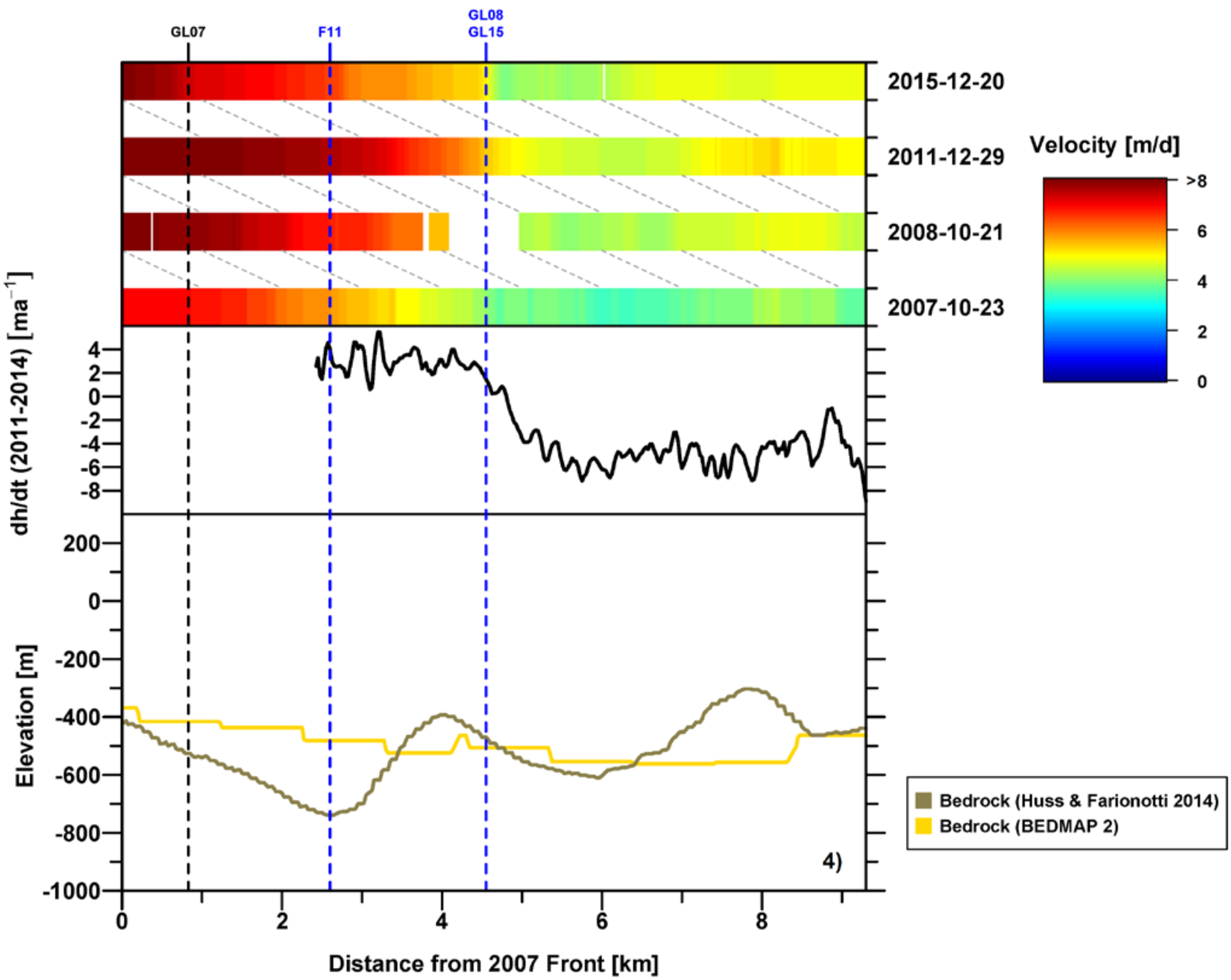

At the lower part of Fleming Glacier, the velocity data and a pronounced change in the elevation change rates extracted along Profile 4 (Fig. 6) indicate that the current GL is located some hundred meters behind a hill chain, visible in the modelled bedrock data ~4 km upstream. A comparable velocity pattern in 2008 suggests that at this time the glacier was already grounded at a similar location. It is likely that the glacier is currently grounded on the hills, but the correct representation of the topography may be distorted in the modeled bedrock data.

References

Bamber, J. and Bentley, C.: A comparison of satellite-altimetry and ice-thickness measurements of the Ross Ice Shelf, Antarctica, Annals of Glaciology, 20, 357–364, 1994.

Benn, D. I. and Evans, D. J. A.: Glaciers & glaciation, Routledge, London, 2013.

Ferrigno, J. G.: Coastal-change and glaciological map of the Larsen Ice Shelf area, Antarctica, 1940-2005, Reston, Va., 2008.

Fretwell, P., Pritchard, H. D., Vaughan, D. G., Bamber, J. L., Barrand, N. E., Bell, R., Bianchi, C., Bingham, R. G., Blankenship, D. D., Casassa, G., Catania, G., Callens, D., Conway, H., Cook, A. J., Corr, H. F. J., Damaske, D., Damm, V., Ferraccioli, F., Forsberg, R., Fujita, S., Gim, Y., Gogineni, P., Griggs, J. A., Hindmarsh, R. C. A., Holmlund, P., Holt, J. W., Jacobel, R. W., Jenkins, A., Jokat, W., Jordan, T., King, E. C., Kohler, J., Krabill, W., Riger-Kusk, M., Langley, K. A., Leitchenkov, G., Leuschen, C., Luyendyk, B. P., Matsuoka, K., Mouginot, J., Nitsche, F. O., Nogi, Y., Nost, O. A., Popov, S. V., Rignot, E., Rippin, D. M., Rivera, A., Roberts, J., Ross, N., Siegert, M. J., Smith, A. M., Steinhage, D., Studinger, M., Sun, B., Tinto, B. K., Welch, B. C., Wilson, D., Young, D. A., Xiangbin, C. and Zirizzotti, A.: Bedmap2: improved ice bed, surface and thickness datasets for Antarctica, The Cryosphere, 7, 375–393, doi: 10.5194/tc-7-375-2013, 2013.

Griggs, J. A. and Bamber, J. L.: Ice shelf thickness over Larsen C, Antarctica, derived from satellite altimetry, Geophys. Res. Lett., 36, doi: 10.1029/2009GL039527, 2009.

Griggs, J. A. and Bamber, J. L.: Antarctic ice-shelf thickness from satellite radar altimetry, Journal of Glaciology, 57, 485–498, doi: 10.3189/002214311796905659, 2011.

Huss, M. and Farinotti, D.: A high-resolution bedrock map for the Antarctic Peninsula, The Cryosphere, 8, 1261–1273, doi: 10.5194/tc-8-1261-2014, 2014.

McNabb, R. W., Hock, R., O'Neel, S., Rasmussen, L. A., Ahn, Y., Braun, M., Conway, H., Herreid, S., Joughin, I., Pfeffer, W. T., Smith, B. E. and Truffer, M.: Using surface velocities to calculate ice thickness and bed topography. A case study at Columbia Glacier, Alaska, USA, Journal of Glaciology, 58, 1151–1164, doi: 10.3189/2012JoG11J249, 2012.

Seehaus, T., Marinsek, S., Helm, V., Skvarca, P. and Braun, M.: Changes in ice dynamics, elevation and mass discharge of Dinsmoor–Bombardier–Edgeworth glacier system, Antarctic Peninsula, Earth and Planetary Science Letters, 427, 125–135, doi: 10.1016/j.epsl.2015.06.047, 2015.

Wendt, J., Rivera, A., Wendt, A., Bown, F., Zamora, R., Casassa, G. and Bravo, C.: Recent ice-surface-elevation changes of Fleming Glacier in response to the removal of the Wordie Ice Shelf, Antarctic Peninsula, Annals of Glaciology, 51, 97–102, doi: 10.3189/172756410791392727, 2010.